Chiral Instabilities and the Onset of Chiral Turbulence in QED Plasmas

Mark Mace,[1,2,*] Niklas Mueller,[3,†] Sören Schlichting,[4,‡] and Sayantan Sharma[5,§]
[1]*Department of Physics, University of Jyväskylä, P.O. Box 35, 40014 Jyväskylä, Finland*
[2]*Helsinki Institute of Physics, University of Helsinki, P.O. Box 64, 00014 Helsinki, Finland*
[3]*Physics Department, Brookhaven National Laboratory, Building 510A, Upton, New York 11973, USA*
[4]*Fakultät für Physik, Universität Bielefeld, D-33615 Bielefeld, Germany*
[5]*The Institute of Mathematical Sciences, HBNI, Chennai 600113, India*

(Received 18 October 2019; accepted 16 April 2020; published 15 May 2020)

We present a first principles study of chiral plasma instabilities and the onset of chiral turbulence in QED plasmas with strong gauge matter interaction ($e^2N_f = 64$), far from equilibrium. By performing classical-statistical lattice simulations of the microscopic theory, we show that the generation of strong helical magnetic fields from a helicity imbalance in the fermion sector proceeds via three distinct phases. During the initial linear instability regime the helicity imbalance of the fermion sector causes an exponential growth (damping) of magnetic field modes with right- (left-) handed polarization, for which we extract the characteristic growth (damping) rates. Secondary growth of unstable modes accelerates the helicity transfer from fermions to gauge fields and ultimately leads to the emergence of a self-similar scaling regime characteristic of a decaying turbulence, where magnetic helicity is efficiently transferred to macroscopic length scales. Within this turbulent regime, the evolution of magnetic helicity spectrum can be described by an infrared power spectrum with spectral exponent $\kappa = 10.2 \pm 0.5$ and dynamical scaling exponents $\alpha = 1.14 \pm 0.50$ and $\beta = 0.37 \pm 0.13$.

DOI: 10.1103/PhysRevLett.124.191604

Novel macroscopic phenomena related to the in- and out-of-equilibrium dynamics of chiral fermions have inspired a significant amount of theoretical and experimental developments in recent years. By means of the chiral magnetic effect (CME) [1–8], one hopes, for example, to investigate the topological structure of quantum chromodynamics (QCD) in ultrarelativistic heavy ion collisions [9,10]; or explore new kinds of transport phenomena in condensed matter systems [11–14], including dissipationless electric transport in Dirac and Weyl semimetals [12,15,16], as well as applications to optoelectronics [17–19].

One important aspect of anomalous transport concerns the question how chirality is transferred between gauge fields and fermionic degrees of freedom. While in QCD plasmas, chirality transfer can be efficiently accomplished by sphaleron transitions between different topological sectors of the non-Abelian gauge theory [20], the situation is markedly different in Abelian plasmas. Quantum electrodynamics (QED) is topologically trivial and a different mechanism has to be invoked to convert fermionic chirality into magnetic helicity (and vice versa). In this context, a novel type of "chiral" plasma instability has been suggested as a viable mechanism, whereby a chirality imbalance in the fermion sector can generate helical magnetic fields that exist on macroscopic length scales [21,22].

Such effects have been proposed as a possible explanation for the creation of large scale helical magnetic fields in astrophysical systems, such as supernovae and compact stars [23–28], or in primordial plasmas of the early Universe [29–33] where the interplay between fermion chirality and magnetic helicity could be responsible for the transport of magnetic helicity from microscopic to macroscopic scales.

Chiral instabilities in QED plasmas have been studied previously based on different theoretical approaches including magnetohydrodynamics (MHD) [34–41], compact and noncompact lattice QED simulations [42–45], kinetic theory [46,47], linearized perturbation theory [48], and effective action approaches [24,26]. Despite strong theoretical interest, previous studies have come to different conclusions, and there appears to be no general agreement regarding the detailed mechanisms and viability of such a scenario.

In this Letter we present a comprehensive study of chiral instabilities using microscopic real-time lattice simulations of strongly coupled QED plasmas. Starting from a helicity imbalance in the fermion sector, we employ a classical-statistical description [49–53] to simulate the subsequent nonequilibrium evolution of the system from first principles. We demonstrate that chiral instabilities in QED-like theories follow a characteristic pattern of quantum many body systems subject to instabilities [54–59], where the exponential growth of unstable modes leads to the

---

emergence of turbulent behavior. Based on our microscopic simulations, we are able to characterize the entire sequence of events, starting from the extraction of growth (and decay) rates of helical gauge field modes in the primary and secondary instability regimes all the way to the turbulent scaling regime, for which we extract, for the first time, the relevant far-from-equilibrium scaling exponents.

Simulation technique.—We perform real-time simulations of N_f degenerate flavors of quantum Dirac fermions of mass m and charge e, coupled to classical-statistical U(1) gauge fields [60–65]. By numerically solving the coupled set of Dirac equations for fermion fields $\hat{\Psi}_{\mathbf{x}}(t)$

$$i\partial_t \hat{\Psi}_{\mathbf{x}}(t) = \gamma^0(-i\gamma^i D_i[A] + m)\hat{\Psi}_{\mathbf{x}}(t), \tag{1}$$

where $D^i[A] \equiv \partial^i - ieA^i_{\mathbf{x}}(t)$ is the covariant derivative in temporal-axial ($A_0 = 0$) gauge, and Maxwell's equations for electromagnetic fields $\mathbf{E}^i_{\mathbf{x}}(t)$ and $\mathbf{B}^i_{\mathbf{x}}(t)$,

$$\partial_t e\mathbf{E}^i_{\mathbf{x}}(t) - [\nabla \times e\mathbf{B}_{\mathbf{x}}(t)]^i = -e^2 N_f \mathbf{j}^i_{\mathbf{x}}(t), \tag{2}$$

we include the effects of electromagnetic fields on the fermion sector in Eq. (1), as well as the non-linear back-coupling of fermion currents $\mathbf{j}^i_{\mathbf{x}}(t) = \langle \frac{1}{2}[\hat{\bar{\Psi}}_{\mathbf{x}}(\gamma^i, \hat{\Psi}_{\mathbf{x}}(t)]\rangle$, where $\hat{\bar{\Psi}}_{\mathbf{x}} \equiv \hat{\Psi}^\dagger_{\mathbf{x}}\gamma^0$, on the dynamical evolution of the electro-magnetic fields in Eq. (2). We note that the classical-statistical description in Eqs. (1) and (2) is accurate to leading order in the gauge coupling e^2, but to all orders in the coupling between gauge and matter fields e^2N_f [60,62]. We will specifically work in the regime of strong interactions between gauge and matter fields with $e^2N_f = 64$, which is significantly larger than in single flavor QED ($e^2N_f \approx 0.09$), but necessary to resolve all relevant scales on the available size lattices.

We initially prepare the system as a chirally imbalanced charge neutral Fermi gas, by specifying the initial occupation numbers of left- (L) and right- (R) handed fermions according to a Fermi-Dirac distribution $n_F^{L/R}(t = 0, \mathbf{p}) = 1/[e^{(E_{\mathbf{p}} \pm \mu_h)/T} + 1]$ with helicity chemical potential μ_h and energy $E_{\mathbf{p}} = \pm\sqrt{\mathbf{p}^2 + m^2}$ for particles and antiparticles, respectively. We focus on the low-temperature behavior $T/\mu_h = 1/8$ and consider vacuum initial conditions for the electromagnetic field sector, which are represented by a classical-statistical ensemble of fluctuating fields [66].

We discretize the theory on a N_s^3 spatial lattice with lattice spacing a_s, using a compact Hamiltonian lattice formulation of QED [69], with $O(a_s^3)$ tree-level improved Wilson fermions, which as detailed in [65] is crucial for studying effects related to the chiral anomaly. Based on the lattice discretization, the fermion field operator $\hat{\Psi}_{\mathbf{x}}(t)$ becomes finite dimensional, and the solution to the operator Eq. (1) can be constructed from linear combinations of a complete set of $4N_s^3$ wave functions [60,65]. We employ a leap-frog solver with time step $a_t = 0.001a_s$ to solve the discretized equations of motions [(1) and (2)] and study different size lattices $N_s^3 = 32^3, 48^3$ with spacings $\mu_h a_s = 2/3, 1, 1.25, 1.5$ to monitor residual discretization effects. Simulations are performed close to the chiral limit $m \ll \mu_h$ by employing $ma_s = 5 \times 10^{-4}$ and if not stated otherwise we show results for $N_s^3 = 48^3$ and $\mu_h a_s = 1$ expressed in terms of dimensionless quantities in units of the initial helicity chemical potential μ_h. We will use continuum notation throughout the main text and refer to the supplemental material for a detailed description of the corresponding lattice implementation.

Chiral instabilities.—Starting from an initial helicity imbalance ($\mu_h > 0$) in the fermion sector, the chiral plasma instability triggers an exponential growth of gauge fields with right-handed (circular) polarization. Separating the magnetic field into left- and right-handed components according to their helicity projection in Fourier space [70]

$$\mathbf{B}^{L/R}(t, \mathbf{p}) = \frac{|\mathbf{p}| \pm i\mathbf{p}\times}{2|\mathbf{p}|}\mathbf{B}(t, \mathbf{p}), \tag{3}$$

one finds that at early times only the right-handed components experience exponential growth within a narrow momentum range; all other modes show a damped oscillatory behavior as can be qualitatively expected from the interplay of electric-magnetic fields and currents in a conducting medium. This is shown in Fig. 1, where we present the evolution of the occupation numbers of left- and right-handed components of the magnetic fields

$$n_B^{L/R}(t, \mathbf{p}) \equiv |\mathbf{B}^{L/R}(t, \mathbf{p})|^2/|\mathbf{p}|, \tag{4}$$

for selected momentum modes with $|\mathbf{p}|/\mu_h = 0.1$–1.0.

We further quantify this behavior in Fig. 2, where we show the growth rates (blue symbols) for the primary unstable and damping rates (orange symbols) of initially stable modes, extracted from an exponential fit to the

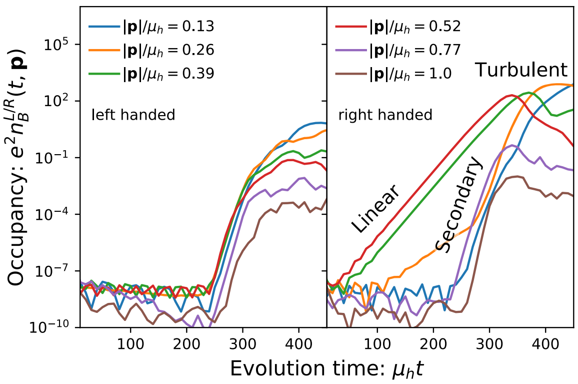

FIG. 1. Evolution of the occupation numbers $n_B^{L/R}(t, \mathbf{p})$ of left-handed (left panel) and right-handed (right panel) magnetic field modes as a function of time $\mu_h t$ for different momenta in the range $|\mathbf{p}|/\mu_h \approx 0.1$–$1.0$. Distinct regimes of linear growth, secondary growth and onset of turbulent behavior are also indicated.

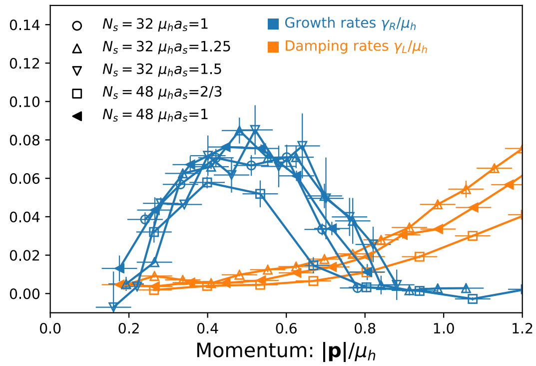

FIG. 2. Growth rates of right-handed (blue symbols) and damping rates of left-handed (orange symbols) magnetic field modes in the linear instability regime.

evolution of the occupation number $n_B^{L/R}(t,\mathbf{p}) \propto \exp(\mp\gamma_{L/R}(|\mathbf{p}|)t)$ in the linear instability regime. Details of the fitting procedure are given in the Supplemental Material [66]. Shown results for the growth and damping rates are quantitatively consistent across different lattices, with a maximal growth rate $\gamma_0 \approx 0.07\mu_h$ for right-handed modes with momenta $|\mathbf{p}| \approx 0.5\mu_h$.

While the exponential growth (damping) of right- (left-) handed modes sets in almost directly after a short delay of $\mu_h t \approx 20$–50 due to the initial quench [71], the evolution continues in this fashion until nonlinear interactions between unstable modes induce secondary instabilities [58,74]. During this second phase, which in Fig. 1 occurs around $\mu_h t \approx 250$, a large range of left- and right-handed momentum modes starts to exhibit exponential growth with strongly enhanced growth rates $\gamma_{\text{secondary}} \sim (2-3)\gamma_0$, until around $\mu_h t_{\text{sat}} \approx 300$ the instability saturates and the exponential growth terminates.

Energy and helicity transfer.—Before we describe the dynamics at later times in more detail, it is insightful to investigate how the conserved quantities are shared and transferred between fermions and gauge field throughout the evolution of the system. Clearly, the total energy density is conserved and can be separated into the contributions from the electromagnetic fields $\varepsilon_g(t) = \int_V\{[\mathbf{E}_\mathbf{x}^2(t)/2] + [\mathbf{B}_\mathbf{x}^2(t)/2]\}$ and the fermion sector $\varepsilon_f(t) = N_f \int_V \langle \frac{1}{2}[\hat{\bar{\Psi}}_\mathbf{x}(t), \gamma^0(-i\gamma^i D_i[A] + m)\hat{\Psi}_\mathbf{x}(t)]\rangle$, where $\int_V = (1/V)\int d^3\mathbf{x}$ denotes volume averages. By means of the axial anomaly relation [75,76]

$$\partial_t n_5(t) = -2N_f \partial_t n_h(t) + 2imN_f \int_V \left\langle \frac{1}{2}[\hat{\bar{\Psi}}_\mathbf{x}(t), \gamma^5 \hat{\Psi}_\mathbf{x}(t))]\right\rangle, \tag{5}$$

one also finds an approximate conservation law for the net chiral charge density of the system, such that the sum of the chiral charge density of fermions

$$n_5(t) = N_f \int_V \left\langle \frac{1}{2}[\hat{\bar{\Psi}}_\mathbf{x}(t), \gamma^0\gamma^5 \hat{\Psi}_\mathbf{x}(t)]\right\rangle, \tag{6}$$

and magnetic helicity,

$$n_h(t) = \frac{e^2}{4\pi^2} \int_0^t dt' \int_V \mathbf{E}_\mathbf{x}(t') \cdot \mathbf{B}_\mathbf{x}(t'), \tag{7}$$

is conserved in the chiral limit ($m \to 0$) and we have checked explicitly that for the small values of m considered, dissipative effects due to finite fermion mass in the second line of Eq. (5) are negligible over the time scale of our simulations.

Simulation results for the individual contributions to the energy density (left panel) and net chirality (right panel) are compactly summarized in Fig. 3. Different points in each panel show the results for different lattice sizes and spacings, and we have shifted the horizontal axis of the individual data sets to account for the residual discretization dependence in the time $\mu_h t_{\text{sat}}$ where exponential growth saturates [77]. While initially the dominant contribution to energy density and net chirality resides in the fermion sector, the chiral plasma instability leads to an exponential growth of electric and magnetic components of the energy density. Growth rates of volume averaged quantities $\mathbf{E}^2(t)$, $\mathbf{B}^2(t)$, and $n_h(t)$ are dominated by the growth rate γ_0 of the maximally unstable mode as indicated by the dashed line $\propto e^{\gamma_0 t}$. Despite the exponential increase, only a small fraction of the total energy density $e^2\varepsilon_{\text{tot}} \approx 0.033 e^2 N_f \mu_h^4$ is transferred from fermions to electromagnetic fields. It is also interesting to observe that throughout the evolution, the magnetic field strength exceeds the electric one by at least one order of magnitude, $\mathbf{B}^2 \gg \mathbf{E}^2$, indicating the presence of strong interactions between gauge and matter fields.

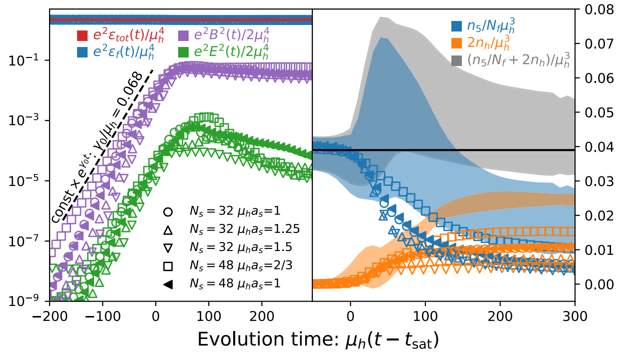

FIG. 3. Evolution of the individual contributions to the energy density $\varepsilon_{\text{tot}}(t)$ (left) and chiral charge density $n_5(t)/N_f + 2n_h(t)$ (right). Different symbols correspond to results obtained using different discretizations $\mu_h a_s = 0.66$–1.5 on $N_s^3 = 32^3, 48^3$ lattices. Shaded bands in the right panel show continuum extrapolations (see the Supplemental Material [66]), which satisfy the anomaly relation in Eq. (5) to good accuracy.

When considering the balance of the net chirality in the plasma, a manifestly different picture emerges. Despite the fact that the (continuum) anomaly relation in Eq. (5) is violated at finite lattice spacing, our use of operator improvements significantly reduces discretization effects, allowing us to perform controlled continuum extrapolations, which are consistent with conservation of the net chirality, as is indicated by the shaded bands in the right panel of Fig. 3. While the continuum extrapolation is subject to relatively large uncertainties due to the available lattice sizes, we can safely infer that a substantial amount of the axial charge density of fermions $n_5(t=0) \approx 0.039\mu_h^3 N_f$ is transferred to magnetic helicity density over the course of the evolution. Specifically, we find that for the two largest lattices available, the magnetic helicity eventually dominates over the axial charge of fermions, i.e., $n_h(t) \gtrsim n_5(t)/N_f$ at late times.

Chiral turbulence.—Subsequent to the saturation of unstable growth, the plasma enters a turbulent regime characterized by a much slower evolution of the system, which we analyze in terms of the (dimensionless) magnetic field and fermion spectra depicted in Fig. 4 at different times $\mu_h t = 100$–600. Spectral distributions of the net helicity in the gauge field sector, i.e., the difference between occupation numbers of left- and right-handed magnetic field modes

$$\Delta n_B(t,\mathbf{p}) = n_B^R(t,\mathbf{p}) - n_B^L(t,\mathbf{p}), \tag{8}$$

are presented in the top panel, whereas the lower panel shows the spectra of left- and right-handed fermions

$$n_F^{L/R}(t,\pm E_{\mathbf{p}}) = \langle \hat{\Psi}^{\dagger}_{\mathbf{p}}(t) u^{\pm}_{L/R}(\mathbf{p}) u^{\pm\dagger}_{L/R}(\mathbf{p}) \hat{\Psi}_{\mathbf{p}}(t) \rangle, \tag{9}$$

extracted from gauged fixed equal time correlation functions of the fermion field $\hat{\Psi}_{\mathbf{p}}(t) = (1/\sqrt{V}) \int_{\mathbf{x}} \hat{\Psi}_{\mathbf{x}}(t) e^{-i\mathbf{p}\cdot\mathbf{x}}$ in Coulomb gauge by performing the appropriate projections onto left- and right-handed helicity spinors $u^{\pm}_{L/R}(\mathbf{p})$ of particles (+) and antiparticles (−).

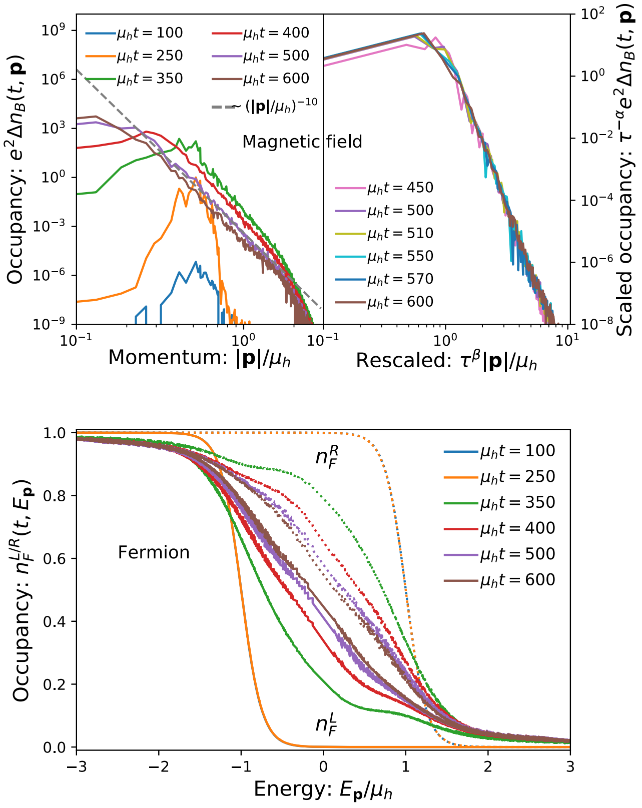

FIG. 4. (top left) Evolution of the net magnetic helicity spectrum $\Delta n_B(t,\mathbf{p})$ during the instability and subsequent turbulent regime. (top right) Self-similarity of the net magnetic helicity spectrum in the turbulent regime, for evolution times $\mu_h t = 450\ldots600$ rescaled according to Eq. (10) with $\alpha = 0.9$, $\beta = 0.3$, and $\mu_h t^* = 375$. (bottom) Evolution of the spectrum $n_F^{L/R}(t,E_{\mathbf{p}})$ of left- or right-handed fermions shows a clear depletion of the axial charge imbalance.

Starting from the linear instability regime for $\mu_h t \lesssim 250$, the net helicity in the gauge sector shows an exponential growth within a limited range of wave numbers $|\mathbf{p}| \lesssim 0.8\mu_h$, while left- and right-handed fermion spectra remain essentially unchanged with distinct sharp Fermi surfaces separated by the helicity chemical potential, shown in the lower panel of Fig. (4). Secondary growth of instabilities between $\mu_h t \approx 250$–300 leads to a strong population of magnetic field modes at low and high wave numbers. Over the same period of time the rapid changes in the gauge field sector are accompanied by a significant heating and depletion of the helicity imbalance in the fermion sector, as can be inferred from the softening of the Fermi surface along with narrowing of the gap between left- and right-handed modes. Eventually, for $\mu_h t \gtrsim 300$, the growth of the chiral instability saturates, and the evolution slows down considerably compared to the rapid changes at earlier times.

In the turbulent regime the spectrum of magnetic helicity $\Delta n_B(t,\mathbf{p})$ exhibits a self-similar scaling behavior, which is illustrated in the top right panel of Fig. 4. Upon rescaling, the spectra at different evolution times $\mu_h t = 450$–600 are all found to collapse onto a single scaling curve $f_s(|\mathbf{p}|)$. While a detailed characterization of the scaling function $f_s(|\mathbf{p}|)$ is beyond the scope of this Letter, we note that for intermediate momenta, the scaling function $f_s(|\mathbf{p}|) \sim |\mathbf{p}|^{-\kappa}$ features a power law behavior with a large scaling exponent $\kappa = 10.2 \pm 0.5$ illustrated by the gray dashed line. Due to self-similarity, the late time evolution of the spectrum of magnetic helicity can be characterized in a compact form

$$e^2\Delta n_B(t,\mathbf{p}) = \tau^{\alpha} f_s(\tau^{\beta}|\mathbf{p}|), \tag{10}$$

with scaling exponents α, β and scaling function f_s, where $\tau \equiv \mu_h(t-t^*)$ is a dimensionless time variable with respect to the reference time $\mu_h t^* \approx 375$ for the transition to the turbulent regime. Notably, a self-similar behavior as in

Eq. (10) is characteristic for the late stage evolution of unstable systems, and has been reported previously in a variety of different contexts [55,78,79]. In all of these examples, the initial instability leads to a rapid memory loss of the initial conditions, such that the subsequent turbulent evolution is universal and entirely characterized by α, β, and f_s, which describe the transport of a conserved quantity across a large separation of scales. Based on a statistical scaling analysis, following the procedures outlined in [79] (see the Supplemental Material [66] for details), we obtain the following estimates for the scaling exponents

$$\alpha = 1.14 \pm 0.50, \qquad \beta = 0.37 \pm 0.13.$$

Since the magnetic helicity density n_h can be equivalently expressed as an integral over the net helicity spectrum $n_h(t) = e^2 \int[(d^3\mathbf{p})/(2\pi)^3]\Delta n_B(t,\mathbf{p})$, one finds that the approximate validity of the scaling relation $\alpha \approx 3\beta$ implies the conservation of the magnetic helicity of the plasma at late times, which is consistent with the behavior seen in Fig. 3. One therefore concludes that the self-similar behavior in Eq. (10) should be associated with an inverse cascade of magnetic helicity, which is transported from microscopic ($\ell \sim \mu_h^{-1}$) to macroscopic length scales ($\ell \sim \mu_h^{-1}\tau^{\beta}$) [80].

Strikingly, the inverse cascade of magnetic helicity also manifests itself directly in the spatial structure of the magnetic field configurations, as illustrated in Fig. 5 where we show stream tracing plots of the magnetic field lines, colored by the relative magnetic field intensity $\mathbf{B}_{\mathbf{x}}^2(t)/\int_V \mathbf{B}_{\mathbf{x}}^2(t)$. Starting from a significant number of small scale swirls at $\mu_h t = 350$ where the unstable growth saturates, one observes a clear coarsening of the magnetic fields towards later times $\mu_h t = 600$, where a few swirls fill the entire simulation volume. It is also evident from Fig. 5 that the QED plasma develops sizeable inhomogeneities over the course of the evolution of the chiral instability, which also manifest themselves in other observables such as, e.g., vector or axial charge densities which are not shown here but will be discussed in a forthcoming publication [81].

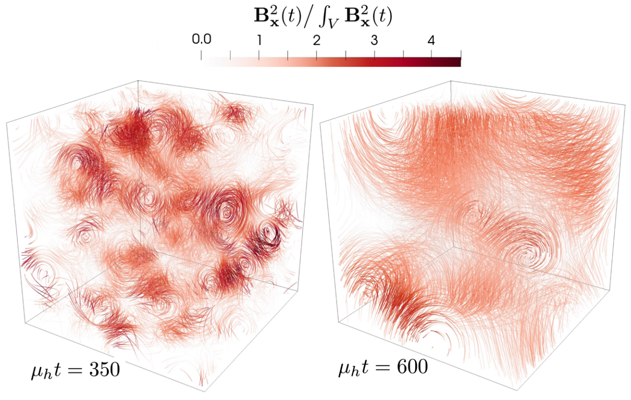

FIG. 5. Visualization of magnetic field lines at times $\mu_h t = 350$ (left) and $\mu_h t = 600$ (right). Coarsening of the magnetic field lines due to the inverse cascade of magnetic helicity is observed.

Conclusions and outlook.—We presented an *ab initio* study of chiral instabilities and chiral turbulence, based on microscopic real-time lattice simulations of strongly coupled QED. Chirality transfer through chiral instabilities and the subsequent generation of macroscopic helical magnetic fields proceeds in a three stage sequence. Initial primary growth is followed by secondary growth until the instability saturates, when the gauge field occupation numbers become nonperturbatively large. During the unstable phase, the fermion chirality is significantly depleted and transferred into magnetic helicity, while most of the energy is still carried by fermions. Subsequently, the system enters a turbulent regime, where magnetic helicity is transported to large distances by an inverse cascade.

While our current study established the dynamics of chiral turbulence close to the chiral limit ($m \ll \mu_h, T$) for strongly coupled QED plasmas ($e^2 N_f \gg 1$), one important next step would be to explicitly verify the universality of our results by varying the coupling strength $e^2 N_f$ and further explore the impact of dissipative effects due to finite fermion mass on the chiral turbulent regime. With regards to the dynamics of the chiral magnetic effect in QCD, it would also be interesting to investigate and compare the analogous dynamics in non-Abelian gauge theories, where one ultimately expects the chirality imbalance in the fermion sector to be absorbed into a nontrivial topology of the non-Abelian gauge fields [20].

We gratefully acknowledge the opportunity to participate in the Intel Knights Landing Hackathon hosted by Brookhaven National Laboratory (BNL) and would like to extend our special thanks to P. Steinbrecher for his help in optimizing the simulation software. The BNL Hackathon was partially supported by the HEP Center for Computational Excellence for Computational Excellence (Grant No. KA24001022) and the SOLLVE Exascale Computing Project (Grant No. 17-SC-20-SC). BNL is supported by the Office of Science of the U.S. Department of Energy under Contract No. DE-SC0012704. We would like to thank the Institute for Nuclear Theory at the University of Washington and the ITP Heidelberg for their kind hospitality during the completion of this work. M. M. was supported by the European Research Council Grant No. ERC-2015-CoG-681707. N. M. is supported by the U.S. Department of Energy, Office of Science, Office of Nuclear Physics, under Contract No. DE-SC0012704 and by the Deutsche Forschungsgemeinschaft (DFG, German Research Foundation)—Project No. 404640738. Sa. S. gratefully acknowledges partial support from the Department of Science and Technology, Government of India, through a Ramanujan fellowship and from the Institute of Mathematical Sciences. This research used resources of the National Energy Research Scientific Computing Center (NERSC), a U.S. Department of Energy Office of Science User Facility operated under Contract No. DE-AC02-05CH11231.

---

[*] mark.f.mace@gmail.com
[†] nmueller@bnl.gov
[‡] sschlichting@physik.uni-bielefeld.de
[§] sayantans@imsc.res.in

[1] D. E. Kharzeev, L. D. McLerran, and H. J. Warringa, Nucl. Phys. **A803**, 227 (2008).

[2] K. Fukushima, D. E. Kharzeev, and H. J. Warringa, Phys. Rev. D **78**, 074033 (2008).

[3] D. E. Kharzeev, K. Landsteiner, A. Schmitt, and H.-U. Yee, Lect. Notes Phys. **871**, 1 (2013).

[4] D. E. Kharzeev, J. Liao, S. A. Voloshin, and G. Wang, Prog. Part. Nucl. Phys. **88**, 1 (2016).

[5] V. Koch, S. Schlichting, V. Skokov, P. Sorensen, J. Thomas, S. Voloshin, G. Wang, and H.-U. Yee, Chin. Phys. C **41**, 072001 (2017).

[6] A. Avkhadiev and A. V. Sadofyev, Phys. Rev. D **96**, 045015 (2017).

[7] Y. Hirono, D. E. Kharzeev, and A. V. Sadofyev, Phys. Rev. Lett. **121**, 142301 (2018).

[8] F. Becattini, L. P. Csernai, and D. J. Wang, Phys. Rev. C **88**, 034905 (2013); **93**, 069901(E) (2016).

[9] F. R. Klinkhamer and N. S. Manton, Phys. Rev. D **30**, 2212 (1984).

[10] R. F. Dashen, B. Hasslacher, and A. Neveu, Phys. Rev. D **10**, 4138 (1974).

[11] P. Hosur and X. Qi, C. R. Phys. **14**, 857 (2013).

[12] Q. Li, D. E. Kharzeev, C. Zhang, Y. Huang, I. Pletikosic, A. V. Fedorov, R. D. Zhong, J. A. Schneeloch, G. D. Gu, and T. Valla, Nat. Phys. **12**, 550 (2016).

[13] A. J. Mizher, A. Raya, and C. Villavicencio, Nucl. Part. Phys. Proc. **270–272**, 181 (2016).

[14] E. V. Gorbar, V. A. Miransky, I. A. Shovkovy, and P. O. Sukhachov, Fiz. Nizk. Temp. **44**, 635 (2017) [Low Temp. Phys. **44**, 487 (2018)].

[15] D. T. Son and B. Z. Spivak, Phys. Rev. B **88**, 104412 (2013).

[16] X. Huang *et al.*, Phys. Rev. X **5**, 031023 (2015).

[17] D. Yudin, O. Eriksson, and M. I. Katsnelson, Phys. Rev. B **91**, 075419 (2015).

[18] C.-K. Chan, P. A. Lee, K. S. Burch, J. H. Han, and Y. Ran, Phys. Rev. Lett. **116**, 026805 (2016).

[19] S. Kaushik, D. E. Kharzeev, and E. J. Philip, Phys. Rev. B **99**, 075150 (2019).

[20] L. D. McLerran, E. Mottola, and M. E. Shaposhnikov, Phys. Rev. D **43**, 2027 (1991).

[21] A. Vilenkin, Phys. Rev. D **22**, 3080 (1980).

[22] Y. Akamatsu and N. Yamamoto, Phys. Rev. Lett. **111**, 052002 (2013).

[23] A. Ohnishi and N. Yamamoto, arXiv:1402.4760.

[24] D. Grabowska, D. B. Kaplan, and S. Reddy, Phys. Rev. D **91**, 085035 (2015).

[25] M. Kaminski, C. F. Uhlemann, M. Bleicher, and J. Schaffner-Bielich, Phys. Lett. B **760**, 170 (2016).

[26] D. B. Kaplan, S. Reddy, and S. Sen, Phys. Rev. D **96**, 016008 (2017).

[27] S. Sen and N. Yamamoto, Phys. Rev. Lett. **118**, 181601 (2017).

[28] M. M. Anber and E. Sabancilar, Phys. Rev. D **96**, 023501 (2017).

[29] D. T. Son, Phys. Rev. D **59**, 063008 (1999).

[30] A. Boyarsky, J. Frohlich, and O. Ruchayskiy, Phys. Rev. Lett. **108**, 031301 (2012).

[31] A. Boyarsky, O. Ruchayskiy, and M. Shaposhnikov, Phys. Rev. Lett. **109**, 111602 (2012).

[32] A. Brandenburg, J. Schober, I. Rogachevskii, T. Kahniashvili, A. Boyarsky, J. Frohlich, O. Ruchayskiy, and N. Kleeorin, Astrophys. J. **845**, L21 (2017).

[33] D. Kharzeev, E. Shuryak, and I. Zahed, arXiv:1906.04080.

[34] L. Campanelli, Phys. Rev. Lett. **98**, 251302 (2007).

[35] A. Brandenburg, T. Kahniashvili, and A. G. Tevzadze, Phys. Rev. Lett. **114**, 075001 (2015).

[36] K. Tuchin, Phys. Rev. C **91**, 064902 (2015).

[37] P. Pavlović, N. Leite, and G. Sigl, Phys. Rev. D **96**, 023504 (2017).

[38] N. Yamamoto, Phys. Rev. D **93**, 125016 (2016).

[39] I. Rogachevskii, O. Ruchayskiy, A. Boyarsky, J. Fröhlich, N. Kleeorin, A. Brandenburg, and J. Schober, Astrophys. J. **846**, 153 (2017).

[40] J. Schober, I. Rogachevskii, A. Brandenburg, A. Boyarsky, J. Fröhlich, O. Ruchayskiy, and N. Kleeorin, Astrophys. J. **858**, 124 (2018).

[41] L. Del Zanna and N. Bucciatini, Mon. Not. R. Astron. Soc. **479**, 657 (2018).

[42] P. V. Buividovich and M. V. Ulybyshev, Phys. Rev. D **94**, 025009 (2016).

[43] D. G. Figueroa and M. Shaposhnikov, J. High Energy Phys. 04 (2018) 026.

[44] D. G. Figueroa and M. Shaposhnikov, Nucl. Phys. **B926**, 544 (2018).

[45] D. G. Figueroa, A. Florio, and M. Shaposhnikov, J. High Energy Phys. 10 (2019) 142.

[46] C. Manuel and J. M. Torres-Rincon, Phys. Rev. D **92**, 074018 (2015).

[47] M. Dvornikov and V. B. Semikoz, Phys. Rev. D **92**, 083007 (2015).

[48] Y. Kojima and Y. Miura, Prog. Theor. Exp. Phys. **2019**, 043E01 (2019).

[49] A. Polkovnikov, Ann. Phys. (Amsterdam) **325**, 1790 (2010).

[50] J. Berges, S. Schlichting, and D. Sexty, Phys. Rev. D **86**, 074006 (2012).

[51] A. Kurkela and G. D. Moore, Phys. Rev. D **86**, 056008 (2012).

[52] S. Jeon, Ann. Phys. (Amsterdam) **340**, 119 (2014).

[53] J. Berges, arXiv:1503.02907.

[54] S. Nazarenko *Wave Turbulence* (Springer, Berlin Heidelberg, 2011).

[55] R. Micha and I. I. Tkachev, Phys. Rev. D **70**, 043538 (2004).

[56] D. Boyanovsky, H. J. de Vega, R. Holman, and J. F. J. Salgado, Phys. Rev. D **54**, 7570 (1996).

[57] R. Micha and I. I. Tkachev, Phys. Rev. Lett. **90**, 121301 (2003).

[58] J. Berges and J. Serreau, Phys. Rev. Lett. **91**, 111601 (2003).
[59] J. Berges, K. Boguslavski, S. Schlichting, and R. Venugopalan, J. High Energy Phys. 05 (2014) 054.
[60] G. Aarts and J. Smit, Nucl. Phys. **B555**, 355 (1999).
[61] J. Berges, D. Gelfand, and J. Pruschke, Phys. Rev. Lett. **107**, 061301 (2011).
[62] V. Kasper, F. Hebenstreit, and J. Berges, Phys. Rev. D **90**, 025016 (2014).
[63] N. Mueller, F. Hebenstreit, and J. Berges, Phys. Rev. Lett. **117**, 061601 (2016).
[64] N. Muller, S. Schlichting, and S. Sharma, Phys. Rev. Lett. **117**, 142301 (2016).
[65] M. Mace, N. Mueller, S. Schlichting, and S. Sharma, Phys. Rev. D **95**, 036023 (2017).
[66] See Supplemental Material at http://link.aps.org/supplemental/10.1103/PhysRevLett.124.191604 for a detailed explanation of the lattice implementation employed and the numerical analysis presented in this manuscript, which includes Refs. [65, 67,68,79].
[67] M. Mace, S. Schlichting, and R. Venugopalan, Phys. Rev. D **93**, 074036 (2016).
[68] G. D. Moore, Nucl. Phys. **B480**, 689 (1996).
[69] J. B. Kogut and L. Susskind, Phys. Rev. D **11**, 395 (1975).
[70] We use $B(t,\mathbf{p}) = (1/\sqrt{V}) \int d^3\mathbf{x} B_{\mathbf{x}}(t) e^{-i\mathbf{p}\cdot\mathbf{x}}$.
[71] Similar findings have been reported in the context of Hard-loop simulations of (Chromo-) Weibel instabilities in anisotropic plasmas, where the delay can be attributed to the formation of current fluctuations and removed by a proper choice of the initial conditions [72,73].
[72] A. Rebhan and D. Steineder, Phys. Rev. D **81**, 085044 (2010).
[73] M. Attems, A. Rebhan, and M. Strickland, Phys. Rev. D **87**, 025010 (2013).
[74] J. Berges and S. Schlichting, Phys. Rev. D **87**, 014026 (2013).
[75] S. L. Adler, Phys. Rev. **177**, 2426 (1969).
[76] J. S. Bell and R. Jackiw, Nuovo Cimento A **60**, 47 (1969).
[77] Saturation times t_{sat} vary between 240 for $\mu_h a_s = 1.5$ and 375 for $\mu_h a_s = 0.66$ (see Ref. [66]), but are approximately independent of the lattice volume.
[78] C.-M. Schmied, A. N. Mikheev, and T. Gasenzer, Int. J. Mod. Phys. A **34**, 1941006 (2019).
[79] J. Berges, K. Boguslavski, S. Schlichting, and R. Venugopalan, Phys. Rev. D **89**, 114007 (2014).
[80] In order to exclude the possibility that the inverse cascade may occurs due to artificial nonlinearities introduced by the lattice formulation, we have verified explicitly that the inverse cascade does not occur when the gauge matter interaction is switched off at intermediate simulation times. Instead the resulting gauge field spectrum remains approximately time independent as expected for noninteracting electromagnetic fields.
[81] M. Mace, N. Mueller, S. Sharma, and S. Schlichting (to be published).